IOP Publishing Nanotechnology
Nanotechnology 28 (2017) 345702 (11pp) https://doi.org/10.1088/1361-6528/aa79ea

Investigating the impact of SEM chamber conditions and imaging parameters on contact resistance of *in situ* nanoprobing

Juntian Qu[1], Martin Lee[2], Michael Hilke[2] and Xinyu Liu[1]

[1] Department of Mechanical Engineering, McGill University, QC H3A 0C3, Canada
[2] Department of Physics, McGill University, Montreal, QC, H3A 2T8, Canada

E-mail: xinyu.liu@mcgill.ca

Received 17 April 2017, revised 7 June 2017
Accepted for publication 15 June 2017
Published 24 July 2017

Abstract

In this paper, we investigate the impact of vacuum chamber conditions (cleanliness level and vacuum pressure) and imaging parameters (magnification and acceleration voltage) of scanning electron microscopy (SEM) on the contact resistance of two-point *in situ* nanoprobing of nanomaterials. Using two typical types of conductive nanoprobe, two-point nanoprobing is performed on silicon nanowires, during which changing trends of the nanoprobing contact resistance with the SEM chamber conditions and imaging parameters are quantified. The mechanisms underlying the experimental observations are also explained. Through systematically adjusting the experimental parameters, the probe-sample contact resistance is significantly reduced from the mega-ohm level to the kilo-ohm level. The experimental results can serve as a guideline to evaluate electrical contacts of nanoprobing and instruct how to reduce the contact resistance in SEM-based, two-point nanoprobing.

Supplementary material for this article is available online

Keywords: *in situ* nanoprobing, contact resistance, SEM chamber conditions, SEM imaging parameters, SEM-based nanomanipulation

(Some figures may appear in colour only in the online journal)

1. Introduction

Over the past two decades, a variety of novel nanomaterials and nanostructures (e.g., 0D nanodots, 1D nanowires/tubes, 2D atomically-thin nanosheets, and 3D hierarchical nanostructures) have emerged as functional building blocks for constructing new types of electronic nanodevice [1, 2], thanks to their unique electrical properties. However, the assessment of their electrical properties is still challenging because of the technical difficulty in establishing low-resistance electrical contacts with these nanostructures [3].

There are two types of experimental method for establishing electrical contacts with a nanostructure: (i) fabrication of metal contact electrodes, and (ii) direct electrical nanoprobing. For fabricating contact electrodes, the most common approach is through electron-beam lithography (EBL) [4]. The EBL process is costly and time-consuming, and often has relatively low yield [5–7]. In addition, the chemical treatment for electrode patterning could alter the surface properties of nanomaterials, thus introducing undesired artifacts in the measurement data of the sample's electrical properties. Alternatively, contact electrodes can also be directly 'written' on a nanostructure by ion-beam-induced deposition (IBID) [3] or e-beam-induced deposition (EBID) [8], both of which decompose a gaseous precursor and form metal contact electrodes with the sample [9].

Although these direct-write methods are conceptually straightforward and generally provide higher spacial resolution than EBL [4], they still have several limitations which make them unsuitable for certain types of material characterization experiments. For instance, the IBID method employs a focused ion beam (FIB) with high energy (e.g., 30 KeV), which may alter or damage the sample surface. It has been reported that the deposition of platinum (Pt) electrodes on a silicon (Si) sample by a gallium (Ga) FIB destroyed

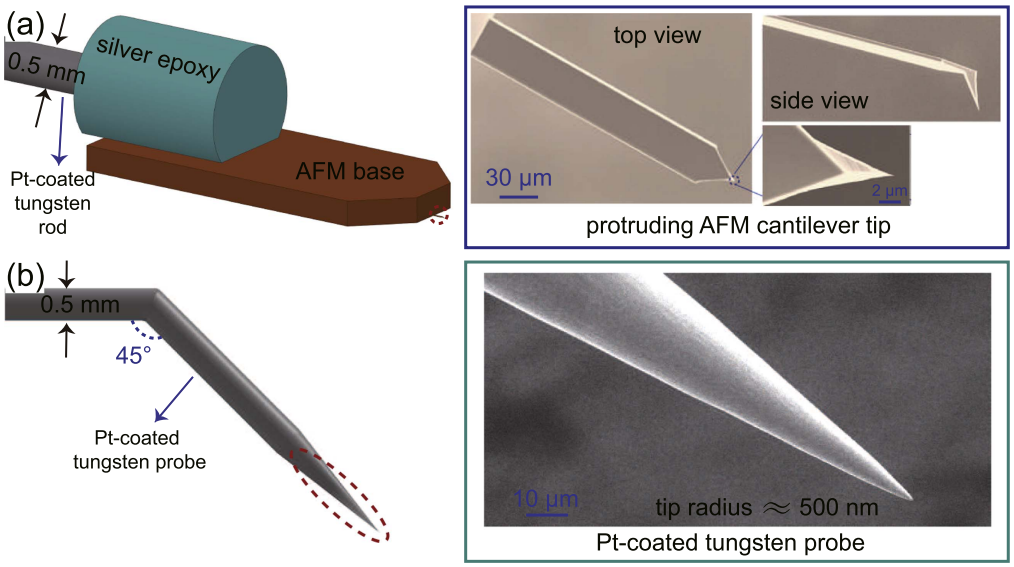

Figure 1. Conductive nanoprobes used in experiments. (a) An AFM nanoprobe with a protruding tip. (b) A tungsten nanoprobe. Both nanoprobes are coated with Pt through sputtering.

crystallinity of the sample and converted it into amorphous Si [3, 10]. Furthermore, the highly energetic Ga ions from the FIB may also cause doping of semiconductor samples, and thus changing their electrical properties [11]. Compared with IBID, EBID is a less destructive process [11], but the composition and electrical property of EBID-deposited metal (e.g., platinum—Pt) electrodes depend on their thickness, resulting in varying electrical contact properties [11].

With the above discussions, the electrical nanoprobing technique is sometimes preferred by certain type of study that requires accurate electrical characterization of as-grown, unaltered nanomaterials [12]. This method uses conductive nanoprobes with nanometer-sized tips to directly probe a sample and establish electrical contacts [13]. For sample imaging, atomic force microscopes (AFMs) [14] or scanning electron microscopes (SEMs) are usually used. An AFM needs to first scan (for visualizing the sample and determining its position) and then probe (for establishing the electrical contact) the sample using the same AFM probe [13, 15]. This process is time-consuming and cannot perform simultaneous sample imaging and nanoprobing. In contrast, a SEM provides much faster sample imaging with nanometer resolution, which greatly facilitates the nanoprobing process [15].

For all the aforementioned methods, the contact resistance between an electrode/nanoprobe and a sample could significantly affect the measured current–voltage (I–V) data; therefore, it is highly desired to minimize the contact resistance during electrical characterization of nanomaterials. Several studies have been reported for reducing the contact resistance of metal electrodes (formed by EBL or EBID) through rapid thermal annealing [16], electric current flowing [17], and e-beam irradiation [18].

For nanoprobing, four-point measurement is a widely adopted technique to eliminate the effect of contact resistance, and has been used for quantifying electrical properties of various nanomaterials such as metallic/semiconductive nanowires [19, 20] and carbon nanotubes [21]. However, there are still experimental scenarios in which four-point probing is less feasible for electrical characterization of nanomaterials. For instance, certain types of nanomaterial (e.g., III-nitride nanorods) have relatively low aspect ratios, making it difficult to establish four-point contacts along the sample length. Additionally, to characterize as-grown nanowires vertically attached to their growth substrate, it is more convenient to conduct *in situ* two-point nanoprobing, with one probe on top of a nanowire and the other on the growth substrate [22]. To date, few studies have been reported on experimental methods for reducing the contact resistance in SEM-based, two-point nanoprobing.

In this paper, we experimentally investigate the effect of SEM chamber conditions (i.e., cleanliness level and vacuum pressure) and imaging parameters (i.e., magnification and acceleration voltage) on the contact resistance of two-point nanoprobing. Using Si nanowires as a sample material, we perform *in situ* nanoprobing using two types of conductive nanoprobe: AFM nanoprobes with protruding tips and tungsten nanoprobes, both of which are coated with Pt. We establish an experimental method to extract the probe-sample contact resistance from I–V data sets of multiple two-point nanoprobing measurements on different portions of the same Si nanowire. We quantify changing trends of the nanoprobing contact resistance with SEM chamber conditions and imaging parameters, which will serve as an experimental guideline on how to improve the electrical contacts in SEM-based nanoprobing experiments.

2. Experimental methods

2.1. Preparation of conductive nanoprobes

Two types of typical conductive nanoprobe with different tip sizes were adopted in our experiments, which could be used to probe samples with different sizes. One is an AFM probe

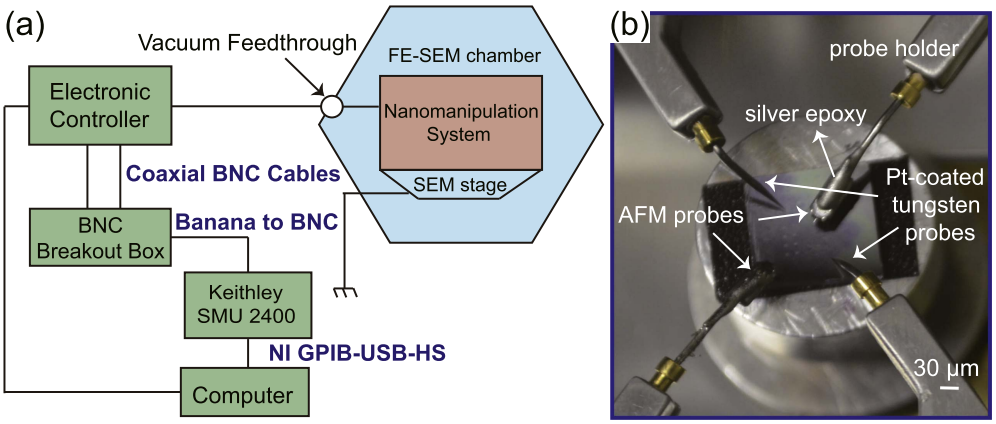

Figure 2. SEM-based nanomanipulation system. (a) Schematic diagram of the system setup. (b) Photograph of two AFM probes and two tungsten nanoprobes, all mounted on the nanomanipulator.

with a protruding tip (ATEC-FM, Nanosensors) of 10 nm in radius, as shown in figure 1(a). The protruding tip can be directly visualized from the top view of a SEM (right of figure 1(a)), which is suited for SEM-based nanoprobing. The other is a tungsten nanoprobe (ST-20-0.5, GGB Industries) with a tip radius of 500 nm, as shown in figure 1(b), which is commonly used in SEM-based nanomanipulation.

Both types of off-the-shelf commercial probe cannot be directly used for electrical nanoprobing because the AFM probe, microfabricated from single crystalline Si, has relatively low conductivity and the tungsten probe usually carries a thin layter of insulating oxide. The conductivity of the nanoprobes can be improved by coating of gold (Au), silver (Ag), or Pt [13], among which Pt coating provides excellent electrical conductivity and wear resistance. We coated a 15 nm layer of Pt on surfaces of the AFM and tungsten probes using a high-vacuum sputtering coater (EM ACE600, Leica), which provides the same group of contact materials (Pt/Si) between the two types of nanoprobe and the nanowire sample. The coated AFM probe was glued onto a Pt-coated tungsten rod (diameter: 0.5 mm; figure 1(a)) via conductive silver epoxy (AA-DUCT 906, Atom Adhesives), and the tungsten rod was finally inserted into a mounting hole of the nanomanipulator for both mechanical and electrical connections. The coated tungsten probe can be directly inserted into the mounting hole of the nanomanipulator (figure 1(b)).

2.2. SEM-based nanomanipulation system

A SEM-based nanomanipulation system (figure 2(a)) was used to perform nanoprobing experiments, which comprises: (i) a field-emission SEM (Quanta 450 FEG, FEI) for sample imaging; (ii) a four-probe piezoelectric nanomanipulator (LF-2000, Toronto Nano Instrumentation), mounted inside the SEM chamber, for driving four conductive probes for sample probing; (iii) a precision source meter (SMU 2400, Keithley) for performing *I*–*V* measurements on a sample; and (iv) a host computer for control of the nanomanipulator and the data acquisition from the source meter. The nanomanipulator includes four separate nanopositioners, each of which has a three-axis coarse positioning stage and a fine positioning stage. A unique advantage of the TNI LF-2000 over other commercial nanomanipulators is that it integrates position feedback (resolution: 0.1 nm) on each of its fine positioning stage, allowing closed-loop-controlled, high-precision nanopositioning. This feature enables accurate positioning and probing of nanowire samples in our experiments.

As shown in figure 2(b), two AFM probes and two tungsten probes are mounted on the nanomanipulator, with the same type of probe facing each other. The electrical cables connecting the four nanoprobes are led out of the SEM chamber through a vacuum feedthrough, and finally fed into the source meter through a custom-made, noise-shielding BNC breakout box (figure 2(a)).

2.3. Conductivity verification of Pt-Coated nanoprobes

To confirm the high conductivity of our Pt-coated nanoprobes, the tips of two nanoprobes of the same type were brought into contact inside the SEM chamber (figure S1(a) is available online at stacks.iop.org/NANO/28/345702/mmedia), and the total resistance between the two cables connecting the two nanoprobes in contact was measured by the source meter. The measured resistance values (figure S1(b)) from the AFM and tungsten probes were compared with that from two high-conductivity commercial nanoprobes (P-100PtIr(P), Unisoku). We found that, the total resistance between two Pt-coated tungsten probes (5.5 Ω) is comparable with that between the high-conductivity commercial nanoprobes (6.6 Ω). The measured resistance data prove the high conductivity of the Pt-coated tungsten probes. The resistance measured from two AFM probes is slightly higher (38.7 Ω) than that of the tungsten probes, which could be caused by the relatively low conductivity of the silver epoxy used for attaching the AFM probe onto the tungsten rod. To verify this, we measured the resistance of the silver epoxy connecting the AFM nanoprobe and the tungsten rod (figure 1(a)) to be 15.8 Ω. Thus, the remaining resistance of the loop of the two AFM nanoprobes without the epoxy is $38.7 - 15.8 \times 2 = 7.1$ Ω, which is at a similar level with that (6.6 Ω) of the high-conductivity commercial probes. Compared with the much higher resistance (in range of KΩ to

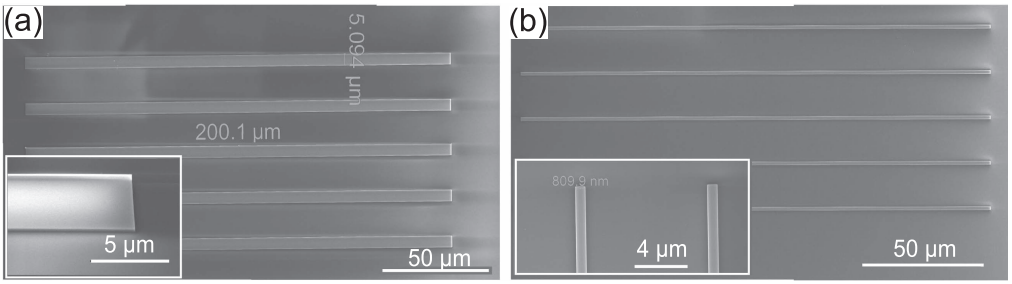

Figure 3. SEM photographs of (a) 5 μm and (b) 800 nm Si nanowires.

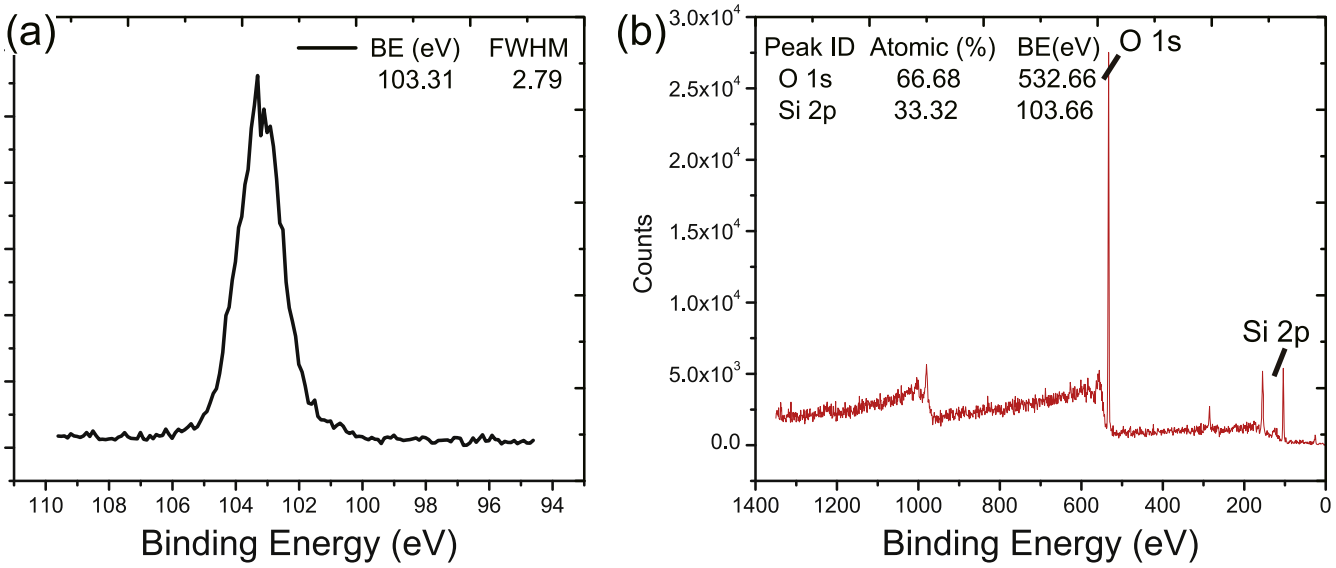

Figure 4. XPS element composition analysis in surrounding areas of Si nanowires. (a) High-resolution XPS spectrum in the energy range of the Si 2p signal. (b) Wide-scan spectrum showing all elements present.

MΩ) of the Si nanowires, the total resistance values of the nanoprobing setup with AFM and tungsten probes could be safely ignored in the following experiments.

2.4. Fabrication and quality assessment of Si nanowires

We selected Si nanowires as the sample material for nanoprobing experiments. Fabrication of silicon nanowires have been well developed using both bottom-up and top-down approaches [23, 24]. The top-down approach such as EBL can predefine the dimensions and locations of Si nanowires on a substrate; therefore, we employed EBL to fabricate the Si nanowires. 200 μm long Si nanowires were fabricated on the device layer (thickness: 220 nm) of a silicon-on-insulator (SOI) wafer through an established EBL process [25], and the detailed fabrication process is shown in figure S2. 5 μm and 800 nm wide nanowires were fabricated, which are probed by the tungsten and AFM nanoprobes, respectively. Figure 3 shows two groups of nanowires of 5 μm and 800 nm in width.

For our nanoprobing experiments, good electrical isolation between two adjacent Si nanowires is essential. To verify if the device layer of the SOI wafer has been completely etched through during nanowire patterning, we carried out element composition analysis (figure 4) in the nanowires surrounding areas (which is supposed to be the SiO_2 layer of the SOI wafer) using x-ray photoelectron spectroscopy–XPS (K-Alpha, Thermo Scientific), right after the EBL patterning. It was confirmed that SiO_2 (binding energy: ~103 eV) is the sole component detected in the surrounding areas of Si nanowires and no residual single crystalline Si was detected on top of the SiO_2 layer, thus proving that adjacent nanowires are electrically isolated by the SiO_2 layer. In addition, we also performed line-scanning energy-dispersive x-ray spectroscopy (EDS) (EDAX, AMETEK) on single Si nanowires to quantify the Si element concentration along the nanowire length. The results (figure 5) reveal uniform Si concentration and thus uniform conductivity along the nanowires.

2.5. Nanoprobing strategy for contact resistance measurement

To experimentally quantify the nanoprobing contact resistance, the transmission-line method (TLM) was employed [26]. The TLM is a rapid, accurate, and cost-effective technique for contact resistance measurement [26], and requires simpler testing structures than the cross-bridge Kelvin resistor structures [27]. It assumes linear dependence of the measured resistance (between the two probes) on the probe spacing (which is true for our Si nanowires with uniform surface conductivity), and involves multiple resistance measurements (at different probe spacings) from which the contact resistance

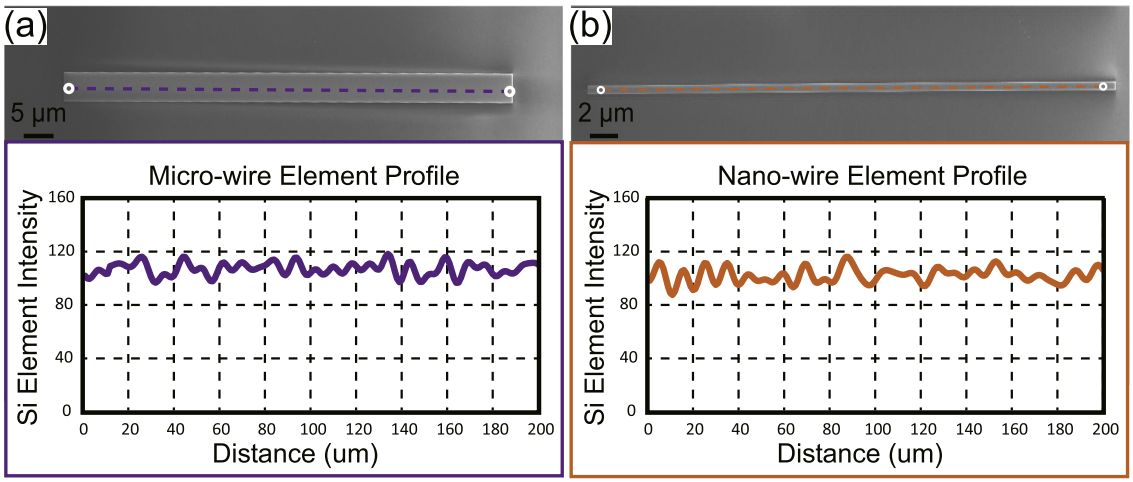

Figure 5. EDS element concentration analysis of (a) 5 μm and (b) 800 nm Si nanowires.

can be extracted [26]. With our experimental setup, the total resistance R_m measured by the source meter includes three components: Si nanowire resistance R_{Si}, two contact resistances $2R_c$ between the probes and the sample, and the remaining total resistance R_p of the two nanoprobes and the electrical connections in the measurement loop. Based on the resistance measurement results in section 2.3, R_p (Ωs) is much lower than R_{Si} and $2R_c$ (kΩ s to MΩ s), and thus can be safely ignored. Therefore,

$$R_m = R_{Si} + 2R_c. \quad (1)$$

The nanowire resistance R_{Si} can be described by:

$$R_{Si} = \frac{\rho_{Si} \cdot L}{T \cdot W} = \frac{R_S}{W} \cdot L, \quad (2)$$

where ρ_{Si} is the resistivity of Si nanowire, T and W are the nanowire thickness and width, L is the probe spacing, and $R_s = \frac{\rho_{Si}}{T}$ is the sheet resistance of Si nanowire (which is constant in this work).

Fitting equation (2) into (1) yields:

$$R_m = \frac{R_S}{W} \cdot L + 2R_c, \quad (3)$$

where the total measured resistance R_m is linearly proportional to the probe spacing L with a slope of $\frac{R_S}{W}$. If we perform multiple measurements of R_m versus L, and the y-intercept of the fitted linear curve of R_m versus L equals to $2R_c$.

In our experiments (figure 6), we first controlled the nanomanipulator to land one of the two nanoprobes onto one end of a Si nanowire, and then employed the other nanoprobe as a 'mobile electrode' to probe the nanowire at four randomly selected locations (circles in figure 6) along the sample length. The 'mobile-electrode' nanoprobe was first landed at the rightmost location with the largest probe spacing, and then moved towards the other probe for the subsequent three probings. At each probe spacing L, the corresponding resistance R_m was measured through I–V scanning of the probed nanowire.

Note that the contact force between the nanoprobe and the nanowire could significantly affect the contact resistance.

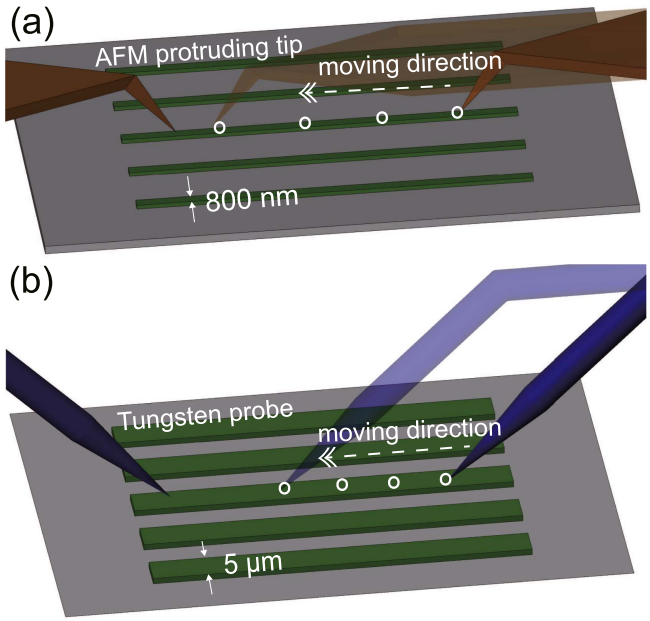

Figure 6. Nanoprobing strategy of Si nanowires of (a) 5 μm and (b) 800 nm width.

To keep our system setup simple, we chose not to include a force sensor for quantifying the contact force. Instead, we controlled the vertical displacement of the nanomanipulator while landing a nanoprobe onto the sample to keep the contact forces relatively consistent. Specifically, we visually detected the contact of the nanoprobe with the nanowire by monitoring the starting point of the nanoprobe sliding on the sample [28], and then further lowered the nanoprobe only by 10 nm. This consistent landing operation ensures a relatively consistent level of contact force. In addition, it has been shown previously that unequally spaced contact points in the TLM provide more accurate measurement results [26], and this is the reason why the four contact points for a single nanowire (figure 6) were randomly selected in our experiments. Also note that the reason why we move the 'mobile-electrode' nanoprobe from the initial rightmost contact location towards the other probe (arrow directions in figure 6) is to

ensure we always probe on intact portions of the nanowire and thus avoid the effect of probing-induced sample damage on the measurement data.

3. Experimental results and discussion

Various experimental conditions could affect the probe-sample contact resistance during SEM-based nanoprobing. In this work, we investigate the impact of SEM chamber conditions (i.e., chamber cleanliness and vacuum pressure) and imaging parameters (i.e., magnification and acceleration voltage) on the contact resistance of Si nanowire probing. We demonstrate that the contact resistance of both types of nanoprobe on the Si nanowires can be significantly reduced through systematic adjustment of the chamber conditions and imaging parameters.

3.1. Impact of SEM chamber conditions

3.1.1. Chamber cleanliness level. Though the SEM vacuum chamber is generally claimed to be a 'clean' environment, there still exists a certain level of hydrocarbon (HC) residues that have not been completely removed by vacuum pumps [29]. Decomposition of the HC by the e-beam irradiation will deposit carbon contaminants on the sample surface [30], which increases the contact resistance of electrical nanoprobing.

The origin of HC contamination can be traced back to mainly three sources: the vacuum pump system, the parts inside the SEM chamber, and the sample itself. Unless the SEM pump is a dry scroll one, it cannot be neglected as a source of HC [31]. Even in many SEMs with turbomolecular pumps, a thin layer of oil can still be observed inside the SEM chamber [31]. SEM parts such as O-rings or stage lubricants can outgas carbonaceous materials into the SEM chamber, and a sample itself can also be a source of HC if it is not washed and handled properly [31].

To examine the impact of chamber cleanliness, we used a plasma cleaner mounted on the SEM to clean the chamber for 10 min, and performed nanoprobing experiments before and after the chamber cleaning (vacuum level: 7.0×10^{-4} Pa for AFM probing and 4.65×10^{-4} Pa for tungsten probing). The SEM imaging parameters were: (i) working distance (WD): 10 mm; (ii) acceleration voltage (V_{acc}): 10 kV; and (iii) magnification: 7500×. To protect the nanomanipulation system (with mounted probes and Si nanowires) from being etched by the cleaning plasma, it was rapidly transferred into the SEM chamber right after cleaning. The entire transfer process took less than 1 min, which minimizes the chance of chamber re-contamination. We also tried to minimize the source of HC from the nanowire sample through cleaning. The sample was first rinsed with acetone and methanol to remove organic contaminants, and then treated with diluted hydrofluoric acid (1.63%) for 60 s to remove any SiO_2 on the Si nanowires.

Figures 7(a) and 8(a) show image sequences of the AFM and tungsten tips probing the 800 nm and 5 μm wide

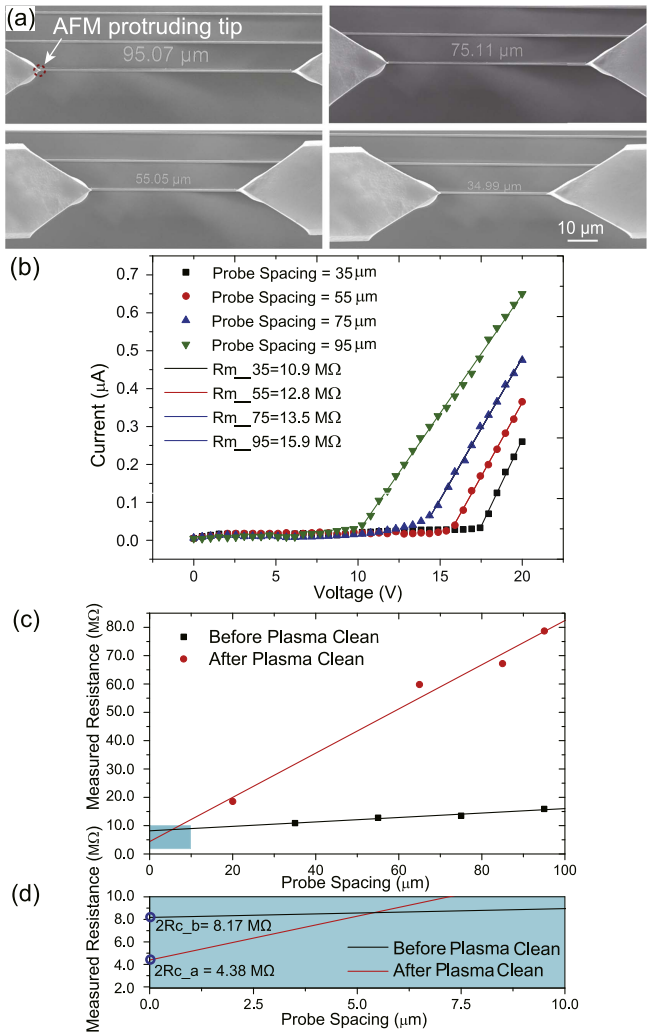

Figure 7. Experimental results of nanoprobing by AFM probes. (a) Image sequence of nanowire probing (top views). (b) Typical *I–V* curves for varying probe spacings before plasma cleaning. The linear portions of the *I–V* curves are fitted to extract the total resistance R_m. (c) Linear curve fitting of the total resistance (R_m) data from four measurements at different probe spacings. (d) Zoomed-in view of the y-intercepts of the linearly fitted curves in (c), which is equal to $2R_c$.

nanowires, respectively. For measuring the total resistance R_m, a voltage sweep from 0 to 20 V was applied to each probed nanowire, during which the *I–V* data were measured. During the resistance measurement, the e-beam was switched off using a beam blanker to avoid electrical noise induced by the incident electrons. Additionally, before each measurement, the nanowire probed by the two nanoprobes were first grounded to eliminate any charge build-up on the sample caused by e-beam irradiation.

Figures 7(b) and 8(b) show the typical *I–V* curves measured before chamber cleaning by the AFM and tungsten nanoprobes, respectively. The nonlinear portion of each *I–V* curve indicates initial Schottky contacts between the nanoprobes and the nanowire, which indicates the existence of certain barrier height defined as the potential difference between the metal (probe coating) vacuum work function and the semiconductor (Si) vacuum electron affinity. Note that

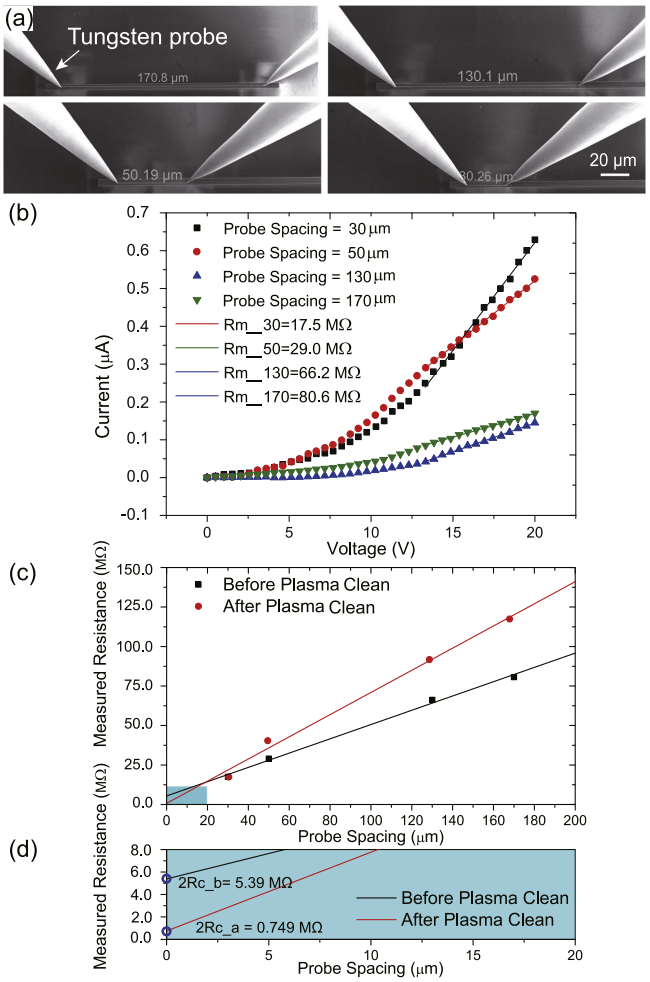

Figure 8. Experimental results of nanoprobing by tungsten probes. (a) Image sequence of nanowire probing (top views). (b) Typical *I–V* curves for varying probe spacings before plasma cleaning. The linear portions of the *I–V* curves are fitted to extract the total resistance R_m. (c) Linear curve fitting of the total resistance (R_m) data from four measurements at different probe spacings. (d) Zoomed-in view of the y-intercepts of the linearly fitted curves in (c), which is equal to $2R_c$.

low-resistance ohmic contact with n-type Si (employed in our SOI wafer) relies on proper choice of the metal material [32] (that is, the vacuum work function of the metal must be close to or smaller than the electron affinity of the Si), a high doping level of the Si [33], and high-temperature annealing of the metal-Si junction [34]. However, in our case, these conditions are not possible to achieve. Firstly, among the metal materials (Au, Ag and Pt) commonly adopted in nanoprobe coating, relatively large Schottky barrier heights exist because of larger vacuum work functions for Au (5.10–5.47 eV), Ag (4.26–4.74 eV), and Pt (5.12–5.93 eV) over the electron affinity of Si (~4.05 eV). We chose Pt for nanoprobe coating because of its good antioxidation nature, high electrical conductivity, and excellent wear resistance. Secondly, the lightly-doped Si device layer (~1 Ω cm) of our SOI wafer does not meet the requirement of highly doping level to achieve ohmic contact. Lastly, though additional annealing step after the metal deposition on Si can improve the contact resistivity (by forming silicide-Si contact), it is not

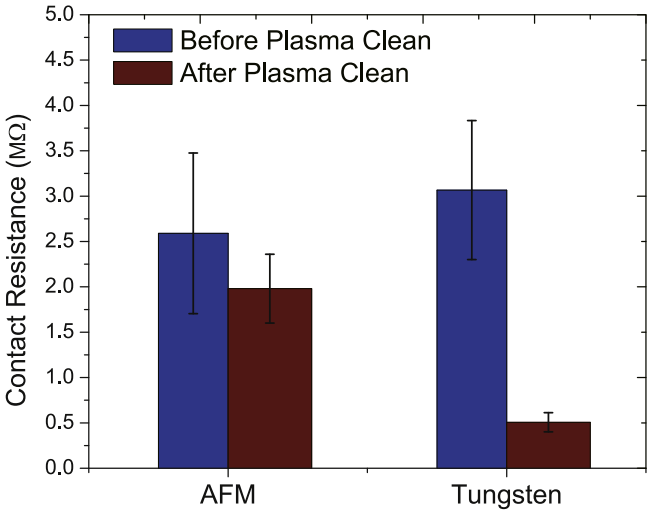

Figure 9. Comparison of contact resistance of the AFM and tungsten probes before and after plasma cleaning ($n = 5$).

applicable to our case of nanoprobing a Si nanowire using a Pt-coated probe. Thus, the *I–V* data of Schottky contact are observed in figures 7(b) and 8(b). When the sweep voltage increases to form a large forward-bias voltage at the contacts, the *I–V* curve becomes a straight line whose inverse slope was equal to R_m. For each nanowire, the resistance values (R_m) from four measurements (at different probe spacings) were fitted into a linear curve (figures 7(c) and 8(c)), whose y-intercept gives $2R_c$ (figures 7(d) and 8(d)).

For each type of nanoprobe, repeated experiments were performed on five nanowires ($n = 5$), and the comparison of the contact resistance values before and after plasma cleaning is shown in figure 9. One can see that, after plasma cleaning, the contact resistance for the AFM probes has been reduced by 23.6%, from 2.59 ± 0.885 MΩ to 1.98 ± 0.380 MΩ. For tungsten probes, the contact resistance has been reduced by 83.5%, from 3.07 ± 0.767 MΩ to 0.507 ± 0.105 MΩ. Based on these data, we conclude that plasma cleaning can effectively reduce the contact resistance of nanoprobing. This is because SEM imaging of the nanowires inside an uncleaned chamber inevitably deposits insulating carbonaceous contaminants onto the nanowires due to the residual HC in the chamber, which causes relatively high contact resistance [35, 36].

3.1.2. Chamber vacuum level. The vacuum level of a SEM chamber is another critical parameter that may affect the electrical nanoprobing. The plasma cleaning method usually cannot completely eliminate the HC contamination [30]; thus, even with chamber cleaning, there still could be HC residues causing contaminant deposition on samples. In this section, we further investigate the impact of the chamber vacuum level on the contact resistance of nanoprobing.

We first plasma-cleaned the SEM chamber for 10 min, and then performed nanoprobing experiments on the Si nanowires at four different vacuum levels in the range of 10^{-3}–10^{-4} Pa (the common vacuum range for the SEM we used). At each vacuum level, the contact resistance was

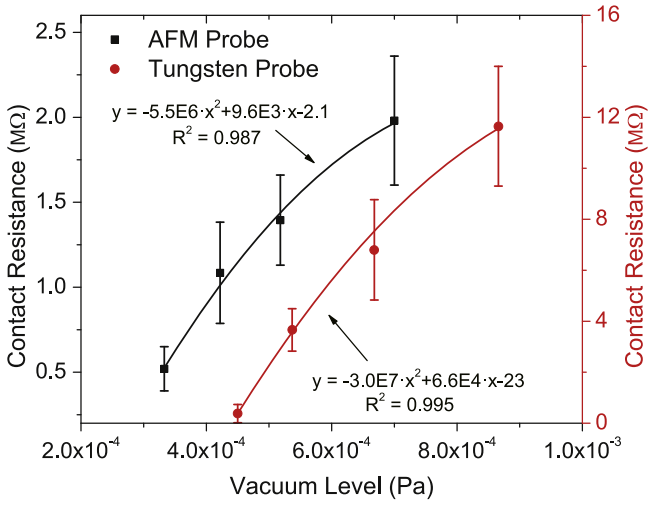

Figure 10. Experimental results of vacuum level impact on nanoprobing ($n = 5$).

measured on five nanowires ($n = 5$), and the same SEM imaging parameters (WD: 10 mm, V_{acc}: 10 kV, magnification: 7500×) were used for all the experiments. The quantitative relationship between the contact resistance and the chamber vacuum level is shown in figure 10.

From the results, we can see that, through second-order polynomial fitting of the measured data points, the contact resistance values from AFM and tungsten probes follow a similar changing trend with the vacuum level. The contact resistance decreases with increased vacuum level, indicating that the probe-sample contact can be significantly improved when a higher vacuum level of the SEM chamber is reached. For tungsten probes, the contact resistance at the highest vacuum level (4.5×10^{-4} Pa) of the vacuum adjustment range is 0.377 ± 0.357 MΩ ($n = 5$), 96.8% lower than that (11.65 ± 2.35 MΩ, $n = 5$) at the lowest vacuum level (8.66×10^{-4} Pa) of the vacuum adjustment range. For AFM probes, the contact resistance at the highest vacuum level (3.33×10^{-4} Pa) of the vacuum adjustment range is 0.52 ± 0.13 MΩ ($n = 5$), 73.7% lower than that (1.98 ± 0.380 MΩ, $n = 5$) at the lowest vacuum level (7.0×10^{-4} Pa) of the vacuum adjustment range.

It has been reported that the thickness of deposited carbonaceous contaminants during SEM imaging depends on the vacuum level of the SEM chamber and a high vacuum level is always desired to mitigate the carbonaceous contamination during *in situ* nanoprobing [35]. This explains the experimental data we observed in figure 10.

Compared with the contact resistance obtained in section 3.1.1 of chamber cleanliness investigation, for tungsten probes (contact resistance after plasma cleaning: 0.507 ± 0.105 MΩ at 4.65×10^{-4} Pa), the contact resistance at the highest vacuum level of 4.5×10^{-4} Pa is 25.6% further reduced; for AFM probes (contact resistance after plasma cleaning: 1.98 ± 0.380 MΩ at 7.0×10^{-4} Pa), the contact resistance at the highest vacuum level of 3.33×10^{-4} Pa is 73.7% further reduced. Through this investigation, we demonstrated that a high vacuum level of the SEM chamber could further reduce the contact resistance after the chamber is cleaned.

3.2. Impact of SEM imaging parameters

Besides the chamber conditions, SEM imaging parameters (e.g., magnification, V_{acc}, WD, and irradiation time) could also affect the electrical contacts of two-point nanoprobing, because all these parameters alter the e-beam irradiation dose (and thus energy) of the sample and thus affect the EBID of carbonaceous contaminants on the sample surface. This type of contaminant deposition occurs even under a relatively high vacuum level of the SEM chamber [36]. Since the imaging magnification and V_{acc} are two common parameters a user adjusts during SEM imaging, we studied their impact on the electrical contact of two-point nanoprobing. For the irradiation time, it is well accepted that it should be kept as short as possible during nanoprobing to minimize the irradiation-induced sample damage and HC deposition. Thus, in our experiments, we kept an approximately constant irradiation time of ~5 min, which is the shortest time a proficient user takes to establish the probe-sample contacts using our SEM setup. The WD is usually kept fixed for a SEM and rarely adjusted by a user. Thus, we fixed it to be 10 mm.

3.2.1. Imaging magnification. For our SEM (Quanta 450 FEG, FEI), the magnification commonly used for SEM nanoprobing ranges from 5500× to 11000×, and the corresponding e-beam spot size number is adjusted from 3.5 to 2.0 accordingly. The magnification and its associated spot size number mainly determine the electron dose of the e-beam delivered to a nanowire sample, and thus affect the amount of HC contaminant deposited to the sample. To our best knowledge, no previous study is reported on experimentally examining the impact of imaging magnification on the contact resistance of nanoprobing.

We performed nanoprobing experiments on the Si nanowires through SEM imaging at four different magnifications (5500×, 7500×, 9500× and 11000×), and the corresponding e-beam spot size numbers were 3.5, 3.0, 2.5 and 2.0, respectively. The adjustment of the e-beam spot size based on the imaging magnification is necessary to ensure sharp SEM vision (without blurring) at different magnifications. Other imaging parameters remained constant in the experiments: WD = 10 mm and V_{acc} = 10 kV. For each *I–V* measurement, we firstly probed a nanowire under the guidance of SEM vision (at a specific magnification), then switched off the e-beam, and connected the two probes contacting the sample to the electrical ground to minimize the charge build-up on the sample. Finally, the *I–V* curve was measured. The TLM was used to extract the contact resistance from four *I–V* data sets obtained at different probe spacings. At each magnification, the contact resistance was measured on five nanowires ($n = 5$), and the quantitative relationship between the contact resistance and the magnification is shown in figure 11.

The contact resistance data, from the AFM and tungsten probes, were fitted by third-order polynomial equations with

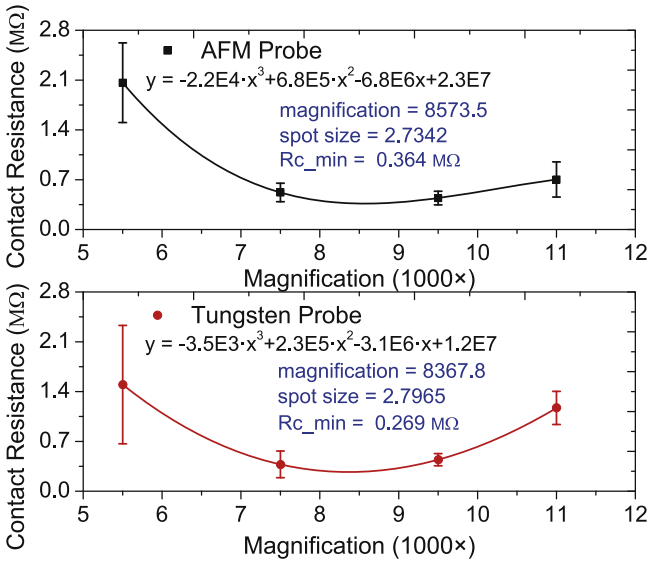

Figure 11. Experimental results of nanoprobing contact resistance versus imaging magnification ($n = 5$), by using (a) AFM and (b) tungsten probes.

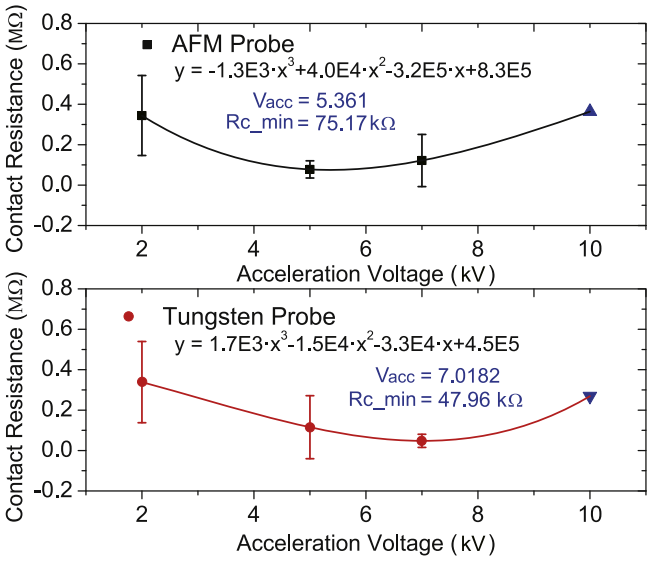

Figure 12. Experimental results of the contact resistance versus acceleration voltage ($n = 5$), by using (a) AFM and (b) tungsten probes. The blue triangles indicate the minimum values of contact resistance obtained from the investigation of the imaging magnification impact.

satisfactory coefficients of determination. The fitted curves of the contact resistance show a similar changing trend with the magnification, and reach their minima at medium levels of magnification. Based on the equations of fitted curves, the lowest contact resistance values are found to be: (i) 0.364 MΩ (magnification: 8574×; spot size: 2.73) for AFM probes; and (ii) 0.269 MΩ (magnification: 8368×; spot size: 2.80) for tungsten probes.

From the data in figure 11, one can observe that, within the range of 5500× to 11000×, too high and too low magnifications both increased the contact resistance. This was caused by the combinatorial effect of the imaging magnification and its associated spot size number. Note that, when the imaging parameters are adjusted, an increase in imaging magnification is associated with a decrease in the e-beam spot size. A higher magnification leads to a smaller area of the sample surface to be scanned by the e-beam, but its associated smaller e-beam spot size number also reduces the total amount of electrons delivered to the scan area of the sample in each scan cycle (which equivalently reduces the total e-beam energy delivered to the sample). Thus, the electron dose delivered to the scan area of the sample during each scan cycle, defined as the amount of electrons per unit scan area, could be high when the magnification is at its low or high end of the range of 5500× to 11000× (when the contribution of the electron amount or the scan area dominates, respectively). It is known that the amount of HC deposition to the sample is proportional to the energy per unit area (proportional to the electron dose) delivered during e-beam scanning [37]; thus, it is well-reasoned that the amount of HC deposition is also proportional to the electron dose delivered to the sample during scanning. This explains the observed changing trend of the contact resistance in figure 11.

To further explain the experimental data, we performed EDS analysis of the carbon concentration (and thus the HC concentration) on the nanowire surface after each nanoprobing experiment. As shown in figures S3 and S4, the measurement curves of carbon concentration well correlate with those of the contact resistance. These data further verify that the change in contact resistance was caused by the change in the amount of HC deposition during SEM imaging.

Through this investigation, we conclude that the imaging magnification and its associated spot size number have a combinatorial effect on the contact resistance of the nanoprobing and a low level of contact resistance can be achieved by adopting a medium level of magnification. Based on the fitted curves of our measurement data, one can see that, compared with the minimal contact resistance values (AFM: 0.52 MΩ, tungsten: 0.377 MΩ), we have achieved while investigating the vacuum level impact, the contact resistance can be further reduced to as low as 0.364 MΩ (magnification: 8574×; spot size: 2.73) for AFM probes and 0.269 MΩ (magnification: 8368×; spot size: 2.80) for tungsten probes.

3.2.2. Acceleration voltage. After investigating the impact of imaging magnification, the optimal imaging magnifications of 8574× (beam spot size: 2.73) for AFM probes and 8368× (beam spot size: 2.80) for tungsten probes were used for experiments probing the impact of the acceleration voltage V_{acc} on the contact resistance. We performed nanoprobing experiments on the Si nanowires at three different acceleration voltages of 2, 5 and 7 kV. At each voltage, the contact resistance was measured on five nanowires ($n = 5$). The quantitative relationship between the contact resistance and acceleration voltage is shown in figure 12, which also includes the contact resistance values at 10 kV (blue triangles) that were obtained in section 3.2.1 (fitted from figure 11).

The experimental results in figure 12 show that the contact resistance data from both the AFM and tungsten probes follow a similar trend with the acceleration voltage. In

the range of 2–10 kV, the contact resistance was high at both the low and high ends of the voltage range, and reached its minimum at a medium level of the acceleration voltage. Through third-order polynomial fitting of the contact resistance data, we found the minimum values of the contact resistance to be: (i) 75.17 KΩ at 5.361 kV for AFM probes, and (ii) 47.96 KΩ at 7.018 kV for tungsten probes, which are 79.4% and 85.9% lower than the highest values in the two contact resistance curves (0.364 MΩ at 10 kV for AFM probes, and 0.339 MΩ at 2 kV for tungsten probes), respectively. Besides, compared with the minimum values of contact resistance (AFM: 0.364 MΩ, tungsten: 0.269 MΩ) we have achieved after the investigation of the imaging magnification impact, the contact resistance has been further reduced by 79.4% and 82.2%, respectively.

The observed trend of the contact resistance as a function of the acceleration voltage, which reflects the deposition level of the HC, can be attributed to the combinatorial effect of the dissociation reaction rate and the deposition rate of HC inside the SEM chamber. A previous theoretical study has shown that low-energy electrons induce a higher rate of the dissociation reaction that generates HC since their energy matches the peak of dissociation cross-section energy of the precursor molecules [38]. On the other hand, the EBID of HC on a sample is a dynamic process, during which the HC molecules arrive at and leave the sample surface simultaneously. It has been demonstrated that the rate of HC deposition primarily depends on the electron dose (which is determined by the period of time the e-beam dwells on the sample and the e-beam current) [36]. Thus, with a fixed scanning time per image frame, a higher acceleration voltage generates a higher e-beam current and thus a higher electron dose, leading to a higher deposition rate of the HC on the sample surface. As the amount of HC deposition depends on both the dissociation reaction and the deposition rate of the HC, the combinatorial effect of these two rates could explain the observed changing trend of the contact resistance we measured, as shown in figure 12.

To further support the measurement data of contact resistance, we performed EDS analysis (figures S5 and S6) of the carbon element concentration on the samples that were nanoprobed under different acceleration voltages. For the EDS analysis, we employed a constant acceleration voltage of 5 kV and a relatively short analysis period of 30 s. Since the period of time for EDS analysis is much shorter than that (5 min) for nanoprobing, the additional HC deposition occurring during the EDS analysis can be safely ignored. From figure S5 and S6, we can see that the carbon element concentrations on different samples show similar trends to those of the measured contact resistance data in figure 12, further validating our experimental observations of the contact resistance as a function of the acceleration voltage.

3.3. Discussion

In this work, we performed a systematic investigation of the impact of the SEM chamber conditions and imaging parameters on the contact resistance of electrical nanoprobing. The two-point *in situ* nanoprobing method adopted in this work can avoid potential modification of sample's electrical properties that may be caused by other methods involving electrode contacts enabled by EBL, IBID, or EBID. In addition, the nanoprobing method allows the the electrical contacts to be established, removed, and re-established at different portions of a nanometer-sized sample, providing high flexibility for electrical characterization of nanomaterials. It could serve as an alternative method to four-point nanoprobing, for testing low-aspect-ratio nanostructures or as-grown nanomaterials for which four-point probing becomes technically challenging.

The experimental results we obtained in this work could serve as a guidance for experimentalists to evaluate and improve the electrical contacts of SEM-based two-point nanoprobing. Note that, as the specific experimental conditions may vary with different system setups, readers are suggested to refer to the experimental methodology presented in this work rather than the contact resistance values that are specific for our experimental setup. In addition, in order to make the proposed experimental method easy to realize and practical for use by common practitioners, we decided not to integrate a micro force sensor in our system for quantifying the contact force. Instead, we controlled the contact force of nanoprobing to be relatively constant by ensuring consistent vertical displacements of the AFM and tungsten probes. If the contact force needs to be quantified in a specific experiment, it is feasible to integrate a micro force sensor (e.g., a piezoresistive self-sensing AFM cantilever) with the nanoprobe, to quantify/control the contact force and examine its effect on the probe-sample contact resistance.

4. Conclusion

This paper reported the experimental investigation of the impact of SEM chamber conditions (cleanliness level and vacuum pressure) and imaging parameters (magnification and acceleration voltage) on the contact resistance value of two-point nanoprobing. After systematically adjusting the chamber parameters and imaging parameters, the contact resistance of tungsten and AFM probes has been reduced from 3.07 MΩ to 47.96 KΩ and from 2.59 MΩ to 75.10 KΩ, respectively. This investigation will serve as a useful guideline to reduce the contact resistance in SEM-based nanoprobing and help improve electrical contacts between the nanoprobes and the sample.

Author contributions

Juntian Qu designed and performed the experiments, analyzed the data, and wrote the paper. Martin Lee contributed to the electron-beam lithography (EBL) layout design and post processing of silicon nanowire samples, and assisted in manuscript preparation. Michael Hilke contributed testing equipment, and supervised the work of Martin Lee. Xinyu Liu designed the experiments, analyzed the data, and wrote the paper.

ORCID

Juntian Qu https://orcid.org/0000-0002-1799-5847
Xinyu Liu https://orcid.org/0000-0001-5705-9765

References

[1] Shen G and Chen D 2010 One-dimensional nanostructures for electronic and optoelectronic devices *Front. Optoelectron. China* **3** 125–38

[2] Tao N 2012 Nanoelectronics, sensors and single molecule biophysics *J. Phys.: Condens. Matter* **24** 160301

[3] Vil A, Hernndez-Ramirez F, Rodrguez J, Casals O, Romano-Rodrguez A, Morante J and Abid M 2006 Fabrication of metallic contacts to nanometre-sized materials using a focused ion beam (FIB) *Mater. Sci. Eng.* C **26** 1063–6

[4] Fauske V, Erlbeck M, Huh J, Kim D, Munshi A, Dheeraj D, Weman H, Fimland B and van Helvoort A 2016 *In situ* electronic probing of semiconducting nanowires in an electron microscope *J. Microsc.* **262** 183–8

[5] Gopal V, Radmilovic V R, Daraio C, Jin S, Yang P and Stach E A 2004 Rapid prototyping of site-specific nanocontacts by electron and ion beam assisted direct-write nanolithography *Nano Lett.* **4** 2059–63

[6] Gopal V, Stach E A, Radmilovic V R and Mowat I A 2004 Metal delocalization and surface decoration in direct-write nanolithography by electron beam induced deposition *Appl. Phys. Lett.* **85** 49–51

[7] Hernandez-Ramirez F, Rodriguez J, Casals O, Russinyol E, Vila A, Romano-Rodriguez A, Morante J and Abid M 2006 Characterization of metal-oxide nanosensors fabricated with focused ion beam FIB *Sensors Actuators* B **118** 198–203

[8] Utke I, Hoffmann P and Melngailis J 2008 Gas-assisted focused electron beam and ion beam processing and fabrication *J. Vac. Sci. Technol.* B **26** 1197–276

[9] Bauerdick S, Linden A, Stampfer C, Helbling T and Hierold C 2006 Direct wiring of carbon nanotubes for integration in nanoelectromechanical systems *J. Vac. Sci. Technol.* B **24** 3144–7

[10] Rubanov S and Munroe P R 2004 FIB-induced damage in silicon *J. Microsc.* **214** 213–21

[11] Chen G, Gallo E M, Burger J, Nabet B, Cola A, Prete P, Lovergine N and Spanier J E 2010 On direct-writing methods for electrically contacting GaAs and Ge nanowire devices *Appl. Phys. Lett.* **96** 223107

[12] Walton A S, Allen C S, Critchley K, Gorzny M L, McKendry J E, Brydson R M D, Hickey B J and Evans S D 2007 Four-probe electrical transport measurements on individual metallic nanowires *Nanotechnology* **18** 065204

[13] Bietsch A, Schneider M A, Welland M E and Michel B 2000 Electrical testing of gold nanostructures by conducting atomic force microscopy *J. Vac. Sci. Technol.* B **18** 1160–70

[14] Hersam M C, Hoole A C F, OShea S J and Welland M E 1998 Potentiometry and repair of electrically stressed nanowires using atomic force microscopy *Appl. Phys. Lett.* **72** 915–7

[15] Kleindiek S, Rummel A, Schock K and Kemmler M 2016 Combining current imaging and electrical probing for fast and reliable *in situ* electrical fault isolation *Proc. European Microscopy Congress, 2016* (Wiley Online Library) (https://doi.org/10.1002/9783527808465.EMC2016.5274)

[16] Lee J-O, Park C, Kim J-J, Kim J, Park J W and Yoo K-H 2000 Formation of low-resistance ohmic contacts between carbon nanotube and metal electrodes by a rapid thermal annealing method *J. Phys. D: Appl. Phys.* **33** 1953

[17] Maki H, Suzuki M and Ishibashi K 2004 Local change of carbon nanotube-metal contacts by current flow through electrodes *J. Appl. Phys.* **43** 2027

[18] Bachtold A, Henny M, Terrier C, Strunk C, Schonenberger C, Salvetat J-P, Bonard J-M and Forro L 1998 Contacting carbon nanotubes selectively with low-ohmic contacts for four-probe electric measurements *Appl. Phys. Lett.* **73** 274–6

[19] Zhang Z, Yao K, Liu Y, Jin C, Liang X, Chen Q and Peng L-M 2007 Quantitative analysis of current–voltage characteristics of semiconducting nanowires: decoupling of contact effects *Adv. Funct. Mater.* **17** 2478–89

[20] Xiao L, Xiao-Bo H, Jun-Ling L, Li G, Qing H, Dong-Xia S and Hong-Jun G 2005 Four-probe scanning tunnelling microscope with atomic resolution for electrical and electro-optical property measurements of nanosystems *Chin. Phys.* **14** 1536

[21] Chen Q, Wang S and Peng L-M 2006 Establishing ohmic contacts for *in situ* current–voltage characteristic measurements on a carbon nanotube inside the scanning electron microscope *Nanotechnology* **17** 1087

[22] Zhao S, Salehzadeh O, Alagha S, Kavanagh K L, Watkins S P and Mi Z 2013 Probing the electrical transport properties of intrinsic inn nanowires *Appl. Phys. Lett.* **102** 073102

[23] Teo B K and Sun X H 2006 From top-down to bottom-up to hybrid nanotechnologies: road to nanodevices *J. Cluster Sci.* **17** 529–40

[24] Hobbs R G, Petkov N and Holmes J D 2012 Semiconductor nanowire fabrication by bottom-up and top-down paradigms *Chem. Mater.* **24** 1975–91

[25] Tseng A A, Chen K, Chen C D and Ma K J 2003 Electron beam lithography in nanoscale fabrication: recent development *IEEE Trans. Electron. Packag. Manuf.* **26** 141–9

[26] Janoch R, Gabor A M, Anselmo A and Dub C E 2015 Contact resistance measurement—observations on technique and test parameters *2015 IEEE 42nd Photovoltaic Specialist Conf. (PVSC)* pp 1–6

[27] Stavitski N, van Dal M J H, Lauwers A, Vrancken C, Kovalgin A Y and Wolters R A M 2008 Systematic TLM measurements of NiSi and PtSi specific contact resistance to n- and p-type Si in a broad doping range *IEEE Electron Device Lett.* **29** 378–81

[28] Ru C, Zhang Y, Sun Y, Zhong Y, Sun X, Hoyle D and Cotton I 2011 Automated four-point probe measurement of nanowires inside a scanning electron microscope *IEEE Trans. Nanotechnol.* **10** 674–81

[29] Vladar A E, Postek M T Jr. and Vane R 2001 Active monitoring and control of electron-beam-induced contamination *Proc. SPIE* **4344** 835–43

[30] Soong C, Woo P and Hoyle D 2012 Contamination cleaning of TEM/SEM samples with the zone cleaner *Micros. Today* **20** 44–8

[31] Postek M T 1996 An approach to the reduction of hydrocarbon contamination in the scanning electron microscope *Scanning* **18** 269–74

[32] Rhoderick E H 1982 Metal-semiconductor contacts *IEE J. Solid-State Electron Devices* **129** 1–14

[33] Yu A 1970 Electron tunneling and contact resistance of metal-silicon contact barriers *Solid-State Electron.* **13** 239–47

[34] Muta H 1978 Electrical properties of platinum-silicon contact annealed in an H_2 ambient *Japan. J. Appl. Phys.* **17** 1089

[35] Zhang D 2010 A nano-tensile testing system for studying nanostructures inside an electron microscope *PhD Thesis* STI, Lausanne

[36] Vladar A and Postek M 2005 Electron beam-induced sample contamination in the sem *Microsc. Microanal.* **11** 08

[37] Griffiths A J V and Walther T 2010 Quantification of carbon contamination under electron beam irradiation in a scanning transmission electron microscope and its suppression by plasma cleaning *J. Phys.: Conf. Ser.* **241** 012017

[38] Rykaczewski K, White W B and Fedorov A G 2007 Analysis of electron beam induced deposition EBID of residual hydrocarbons in electron microscopy *J. Appl. Phys.* **101** 054307